Improving Atmospheric Plasma Spraying of Zirconate Thermal Barrier Coatings Based on Particle Diagnostics

Georg Mauer, Doris Sebold, Robert Vaßen, and Detlev Stöver

Lanthanum zirconate ($La_2Zr_2O_7$) has been proposed as a promising material for thermal barrier coatings. During atmospheric plasma spraying (APS) of $La_2Zr_2O_7$ a considerable amount of La_2O_3 can evaporate in the plasma flame, resulting in a non-stoichiometric coating. As indicated in the phase diagram of the La_2O_3-ZrO_2 system, in the composition range of pyrochlore structure, the stoichiometric $La_2Zr_2O_7$ has the highest melting point and other compositions are eutectic. APS experiments were performed with a TriplexPro™-200 plasma torch at different power levels to achieve different degrees of evaporation and thus stoichiometry. For comparison, some investigations on gadolinium zirconate ($Gd_2Zr_2O_7$) were included, which is less prone to evaporation and formation of non-stoichiometry. Particle temperature distributions were measured by the DPV-2000 diagnostic system. In these distributions, characteristic peaks were detected at specific torch input powers indicating evaporation and solidification processes. Based on this, process parameters can be defined to provide stoichiometric coatings that show good thermal cycling performance.

1. Introduction

Thermal barrier coatings (TBCs) are key elements in the design of advanced gas turbines for both aircraft engines and land-based power generation. They make it possible to achieve the increased gas inlet temperatures required to meet growing demands on improved fuel efficiency, lower emissions, and higher thrust and power (Ref 1). TBC systems consist typically of two layers: a bond coat layer and an insulative ceramic topcoat. The bond coat is often a MCrAlY alloy (M = Co, Ni) and has two major functions. It improves the bonding between the substrate and the topcoat, and it protects the substrate from corrosion and oxidation. The ceramic topcoat

Georg Mauer, Doris Sebold, Robert Vaßen, and **Detlev Stöver**, Institut für Energie- und Klimaforschung (IEK-1), Forschungszentrum Jülich GmbH, Jülich, Germany. Contact e-mail: g.mauer@fz-juelich.de.

provides heat insulation due to its low thermal conductivity resulting from its bulk material characteristics as well as from microstructural features such as pores and voids (Ref 2).

At the end of the 1970s, zirconia stabilized by 6-8 wt.% yttria (YSZ) was established as an almost ideal ceramic topcoat material (Ref 3) because of its high fracture toughness and thermal expansion coefficient. It is deposited by either electron beam physical vapor deposition (EB-PVD) or by atmospheric plasma spraying (APS). YSZ does not form the equilibrium phase (monoclinic and cubic zirconia) during either of the deposition processes but rather a metastable t'-phase due to rapid cooling. It does not significantly transform to the equilibrium phases even at longer operating times and temperatures up to 1200 °C. However, above this temperature limit the material undergoes undesirable diffusion-induced decomposition into high yttria and low yttria phases (Ref 4). While the first of these transforms on cooling to the cubic phase with low toughness, the latter converts to the monoclinic phase which is accompanied by a considerable volume change leading to strains and cracks. Furthermore, above 1200 °C significant sintering occurs, which causes an increase of the Young's modulus affecting the strain tolerance and hence reducing the thermal cycling lifetime (Ref 5, 6).

These shortcomings regarding such elevated turbine gas inlet temperatures have initiated many research activities seeking even better ceramics than YSZ (Ref 7-9). Apart from perovskites, also hexaaluminates, doped zirconia, and ceramics with pyrochlore structure offer very attractive characteristics. In particular, several zirconate pyrochlores show low thermal conductivities as well as high thermal stabilities. Among them, lanthanum zirconate

$La_2Zr_2O_7$ (LZ) is phase stable to its melting point as it can largely tolerate vacancies at the La^{3+}, Zr^{4+}, and O^{2-} sites. At the same time, it displays a lower thermal conductivity (1.56 W m^{-1} K^{-1}, bulk material) and a lower sintering tendency when compared to YSZ. However, the thermal expansion coefficient of 9.1×10^{-6} K^{-1} (30-1000 °C) (Ref 7) is low in relation to bond coats and Ni-base alloy substrates ($\sim 15 \times 10^{-6}$ K^{-1}) and the toughness is poor (Ref 10). The thermal expansion coefficient may be raised by replacing lanthanum by other trivalent rare earth elements having similar ionic radii. This can also lower the thermal conductivity (Ref 11) or even offer the option of temperature sensing by luminescence (Ref 12). However, the problem of low fracture toughness remains crucial. For this reason, pyrochlores are applied in combination with YSZ in double-layer TBC systems (Ref 13, 14). Graded coating systems were also investigated (Ref 15). YSZ is applied as the first ceramic layer since TBC failure is often initiated by cracks occurring close to the bond coat. This YSZ interlayer can, furthermore, prevent possible reactions between the pyrochlore and the alumina-based scale (thermally grown oxide, TGO) formed on the bond coat under thermal load (Ref 16). Here, $LaAlO_3$ was formed above 1200 °C. In contrast, no significant chemical reaction was observed at YSZ LZ interfaces after thermal cycling.

The $La_2O_3 \cdot ZrO_2$ phase diagram shows a stable pyrochlore region up to the melting temperature of 2280 °C (Ref 17). In more recent work a melting point of 2295 ± 10 °C is given (Ref 18). According to the same reference, the stability region ranges from approximately 33 to 35 mol% La_2O_3 at 1500 °C (La/Zr atomic ratio 0.99-1.08). Below the melting temperature, no fluorite phase occurs which is less ordered than the pyrochlore phase. Due to the high fusion enthalpy of ~ 350 kJ mol^{-1}, solidification starts directly in the form of pyrochlore. However, considerable amounts of metastable fluorite phase are formed in the case of rapid solidification, which is typical of plasma spray conditions. Such fluorite phase is transformed to pyrochlore at temperatures above 1000 °C (Ref 19, 20). This is not critical as such transformation is not associated with significant volume change.

The processing of LZ by APS is challenging because La_2O_3 is prone to evaporate in the plasma plume resulting in non-stoichiometric coatings (Ref 16). This might be detrimental for TBC performance as thermophysical properties are affected (Ref 21). Similar problems are known from LZ EB-PVD coatings (Ref 22). La_2O_3 shows considerably higher vapor pressure when compared to ZrO_2 (Ref 23). Although reference data from the literature are not in good agreement, it is evident that the vapor pressure of lanthania is at least one magnitude higher than that of zirconia. Also evaporation rates of La_2O_3 were found to be considerably higher in the temperature range between 2250 and 2500 °C (Ref 24). Evaporation products are LaO, O and O_2 (Ref 25).

Cao et al. (Ref 16) attempted to prevent such non-stoichiometries by adjusting specific excess of La_2O_3 in the powder. It was concluded that the highest La content in the coating is obtained by applying a feedstock with a La/Zr atomic ratio between 1.0 and 1.05. Both at smaller and also larger ratios, less La was detected in the coatings. The reason for this was assumed to be that the evaporation temperature decreases at La_2O_3 contents below and above the compositional existence range of the pyrochlore phase in the same manner as the liquidus line decreases when it approaches the eutectic compositions immediately adjacent on the left and right of this pyrochlore peak. However, no reliable reference data is available on the way in which the evaporation temperature is dependent on the La_2O_3 content.

In the present work, APS experiments were performed with a TriplexPro™-200 plasma torch at different power levels to adjust different degrees of evaporation and thus stoichiometry. The results were verified by chemical, phase, and crystallographic analyses. Although LZ was the focus of this work, some investigations with $Gd_2Zr_2O_7$ (GZ) were also performed for comparison since GZ does not show such a strong tendency to evaporate the rare earth constituent.

Particle temperature distributions were measured in flight by the DPV-2000 diagnostic system. In these distributions, characteristic peaks were detected indicating evaporation and solidification processes. Based on these, as well as on chemical and crystallographic analyses, process parameters can be defined to provide stoichiometric coatings displaying good thermal cycling performance.

2. Experimental

The samples used in this study were coated by APS in a Multicoat facility (Sulzer Metco, Wohlen, Switzerland) with a TriplexPro™ gun mounted on a six-axis robot. The 9 mm diameter nozzle was used with a 1.8 mm diameter feedstock injector. The plasma gas composition was 46 standard liters per minute (slpm) Ar and 4 slpm He. The current was varied between 200 and 525 A yielding plasma torch input powers between 15 and 51 kW. Particle in-flight diagnostics were performed by the DPV-2000 system (TECNAR Automation Ltd., St. Bruno, QC, Canada), which enables particle velocities, temperatures, and diameters to be measured in flight. The operating principles are described elsewhere (Ref 26).

The feedstock was a commercially available LZ powder (Praxair LAO-109, $d_{10} = 7$ μm, $d_{50} = 44$ μm, $d_{90} = 80$ μm) exhibiting a spherical morphology. The powder feed rate was 3.5 g min^{-1} and the carrier gas flow 2.0 slpm Ar. The spray distance was 90 mm and the robot speed 500 mm s^{-1}. The same parameters were applied to process two GZ powders. One was commercially available (Praxair GDO-103, $d_{10} = 25$ μm, $d_{50} = 42$ μm, $d_{90} = 72$ μm) with a spherical morphology; the other one was a fused and crushed (f + c) experimental powder ($d_{10} = 11$ μm, $d_{50} = 18$ μm, $d_{90} = 33$ μm).

Coatings were sprayed on graphite substrates and subsequently stripped by grinding. Parts of the free-standing coatings were used for chemical analysis by

optical emission spectroscopy with inductively coupled plasma (ICP-OES).

The remaining samples were investigated by x-ray diffraction analysis (XRD) and then embedded into epoxy resin to prepare metallographic polished cross sections for microscopic investigation and elemental analysis. XRD was performed on a D4 ENDEAVOR diffractometer (Bruker AXS GmbH, Karlsruhe, Germany) and scanning electron microscope investigation (SEM) on an Ultra55 model (Carl Zeiss NTS GmbH, Oberkochen, Germany) combined with an energy-dispersive x-ray INCAEnergy355 spectrometer (EDS, Oxford Instruments Ltd., Abingdon, Oxfordshire, UK). For SEM examination, the samples were coated with approximately 2 nm platinum. EDS point analysis was performed on LZ samples with an acceleration voltage of 15 kV. Instead of the reference patterns of the EDS system internal database, a polished cross section of LZ feedstock particles was analyzed and defined as standard. The composition of this powder was confirmed by chemical analysis to be almost stoichiometric.

3. Results and Discussion

3.1 Deposition Rate and Chemical Composition

The development of the area-related LZ coating weight for the variation of torch input power between 15 and 51 kW displays a maximum at 21 kW followed by a reduction at higher power (see Fig. 1). This deterioration of the LZ deposition rate (up to ~22 wt.% when related to the maximum) can be explained in part by the evaporation of lanthania (up to ~13 wt.%, see below). The other part is assumed to be caused by decreasing deposition efficiency due to splat fragmentation and bouncing. During the spraying of GZ (f + c), a similar development is observed, however at a higher level because of the different powder morphology. At 51 kW the deposition rate drops for 9 wt.% relative to the maximum; 3 wt.% of which is due to the gadolinia evaporation (see below).

Chemical analysis yields an almost stoichiometric composition of the LZ powder feedstock (33.3 mol%
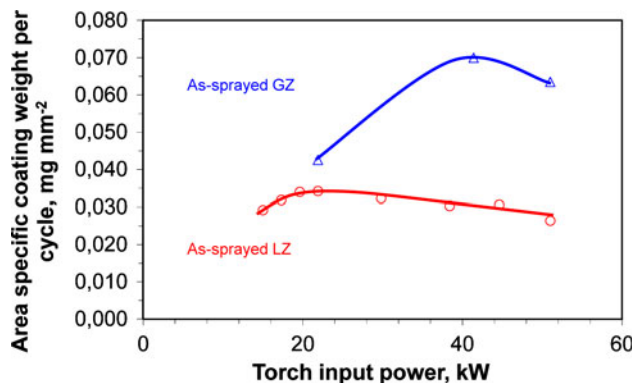
La_2O_3, the La/Zr atomic ratio is nearly 1.0). Moreover, impurities of 0.7 mol% HfO_2, 0.1 mol% CaO, and 0.1 mol% SiO_2 were determined. The GZ powders show moderate gadolinium excess (Gd/Zr ratio is 1.07 and 1.11, respectively).

The lanthania content in the sprayed LZ coatings already exhibits a small initial drop at low torch input power down to 32.9 mol% (La/Zr atomic ratio of 0.99) and if the power is raised it continues to decrease to 27.0 mol% at 51 kW corresponding to a La/Zr atomic ratio of 0.75 (Fig. 2). Here, up to 24.8% of the lanthanum content in the powder feedstock was lost. At the same torch input power, the GZ coatings show a gadolinia content of 30.5 mol% corresponding to a Gd/Zr ratio of 0.89. This means that, relative to the feedstock, 16.8% of the gadolinium was lost. As expected because of the lower vapor pressure of gadolinia, this is less than for LZ. The evaporation of lanthania was confirmed by optical emission spectroscopy revealing strong La and La^+ emission lines in the plasma plume radiation (not shown in this paper).

The La evaporation is in good agreement with the figure of 26% found by Chen et al. in their plasma-sprayed LZ coatings (Ref 21). Based on their reported process conditions, a torch input power of 50 kW can be estimated. Cao et al. (Ref 16) reported a maximum La loss of 13% relative to the content in the feedstock, but at a lower torch input power of 21 kW.

3.2 Phase Composition

XRD analysis of the LZ and GZ feedstock powders yielded solely pyrochlore phases. In the LZ coatings, the content of defective fluorite phase grows as the torch input power is raised. Figure 3 shows x-ray diffractograms of two as-sprayed coatings for low and high torch power. With increasing torch input power, the XRD peaks shift to larger 2θ values indicating the increasing non-stoichiometry. Moreover, the peaks are broadened because of the locally varying stoichiometry. Results of quantitative phase analysis are given in Fig. 4. As the Rietveld analysis (Ref 27) applied for this is based mainly on the weak pyrochlore superlattice reflexes, the absolute results may be subject to errors which are difficult to estimate. However, the trend
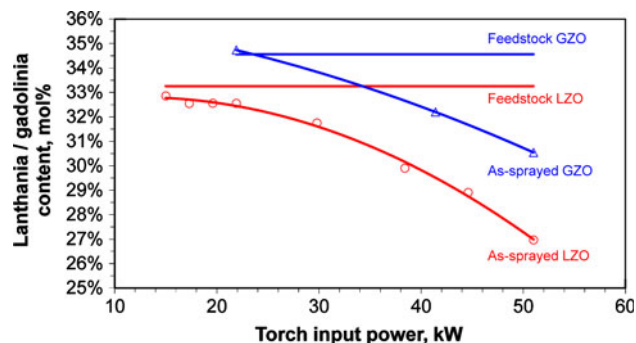

Fig. 1 Area-specific LZ and GZ (f + c powder) coating weight vs. torch input power between 15 and 51 kW

Fig. 2 Lanthania and gadolinia (f + c powder) contents determined by chemical analysis vs. torch input power between 15 and 51 kW
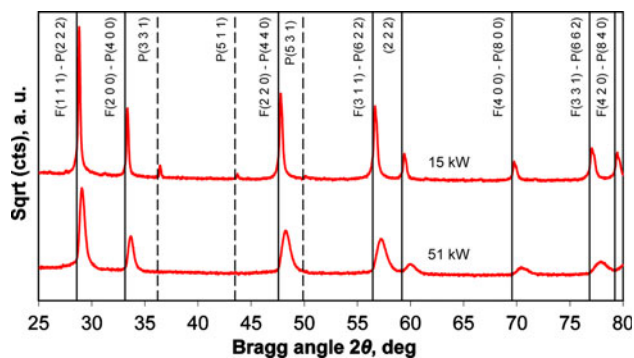
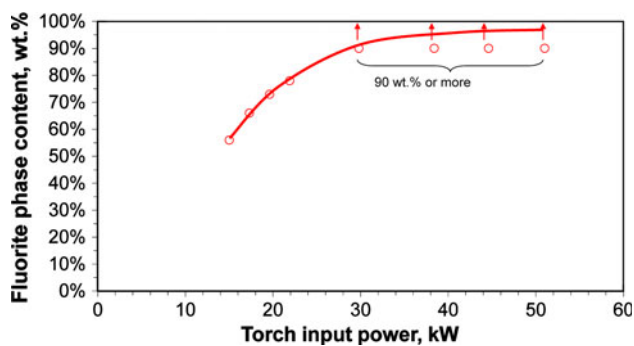**Fig. 3** X-ray diffractograms of two as-sprayed coatings for low and high torch input power

Fig. 4 Fluorite phase content in the as-sprayed LZ coatings determined by XRD vs. torch input power between 15 and 51 kW

Fig. 5 LZ and GZ (f+c powder) fluorite phase lattice parameter determined by Rietveld refinement vs. torch input power between 15 and 51 kW

Fig. 6 Correlation of the LZ and GZ (f+c powder) fluorite phase lattice parameters to the rare earth oxide contents vs. torch input power between 15 and 51 kW

was evident and consistent. At 30 kW and above, the fluorite phase content is 90 wt.% or more, which cannot be differentiated more exactly. In each case, the balance is pyrochlore phase. In the range of XRD detectability, no impurity phases were identified. Obviously, the formation of defective fluorite phase, which is less ordered than the pyrochlore phase, is an effect of the rapid cooling upon impingement on the substrate of such material fractions which are still molten at that time. In contrast, the material fractions which have already solidified during flight may be deposited as pyrochlore.

The GZ coatings show solely defective fluorite phase. According to the phase diagram, solidification starts as fluorite phase. With further cooling, the formation of pyrochlore below approximately 1530 °C is suppressed due to the high cooling rate at deposition on the substrate. Probably, such low temperatures are not reached by any particles still in flight so that pyrochlore phase cannot be formed then.

The Rietveld refinement of the XRD results shows that the lattice parameter of the LZ and GZ fluorite phase decreases with rising torch input power (Fig. 5). The reason for this is the changing stoichiometry due to the evaporation of lanthania and gadolinia. As this varies locally in the coatings (see below), the XRD peaks are increasingly broadened.
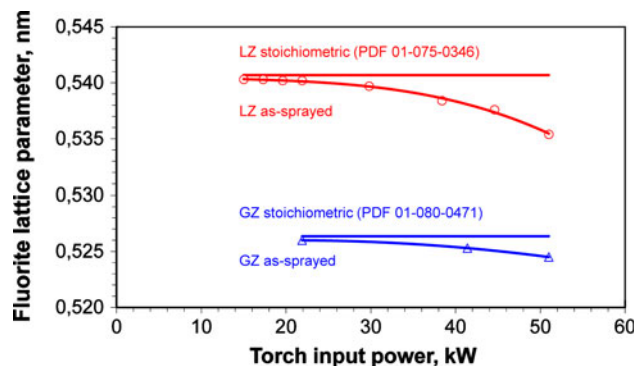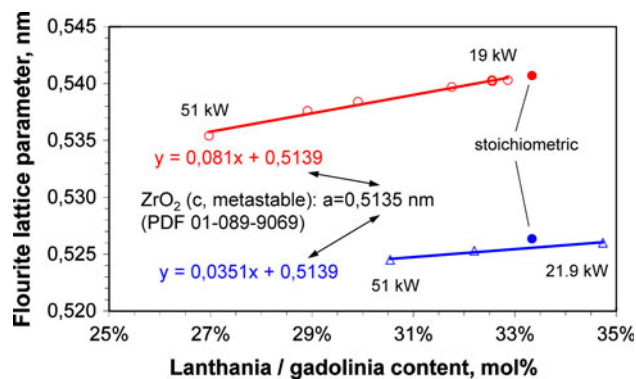
The strong correlation according to Vegard's law (Ref 28) becomes evident if the fluorite lattice parameters are plotted versus the lanthania and gadolinia contents (Fig. 6). The linear equation of the regression lines shows intersections with the vertical axis at zero rare earth content close to the dimensions of the unit cell of meta-stable cubic zirconia, also with fluorite structure. Evidently, with increasing evaporation more rare earth sites are occupied by Zr cations and oxygen vacancies are filled. Thus, the variation of the lattice parameter between pure zirconia and stoichiometric zirconate can be used to estimate the amount of rare earth oxide evaporation.

3.3 Homogeneity of Chemical and Phase Composition

The material contrast of backscattered electron images indicates the uneven stoichiometry. The EDS elemental mapping for oxygen, zirconium and lanthanum in the as-sprayed coating obtained at the highest torch input power of 51 kW confirms that the La/Zr ratio varies considerably. The zirconia-rich areas coincide with splat peripheries (Fig. 7). Similar phenomena are expected for GZ coatings, but to a smaller extent since the gadolinia evaporation is less than for LZ. LZ coatings sprayed at
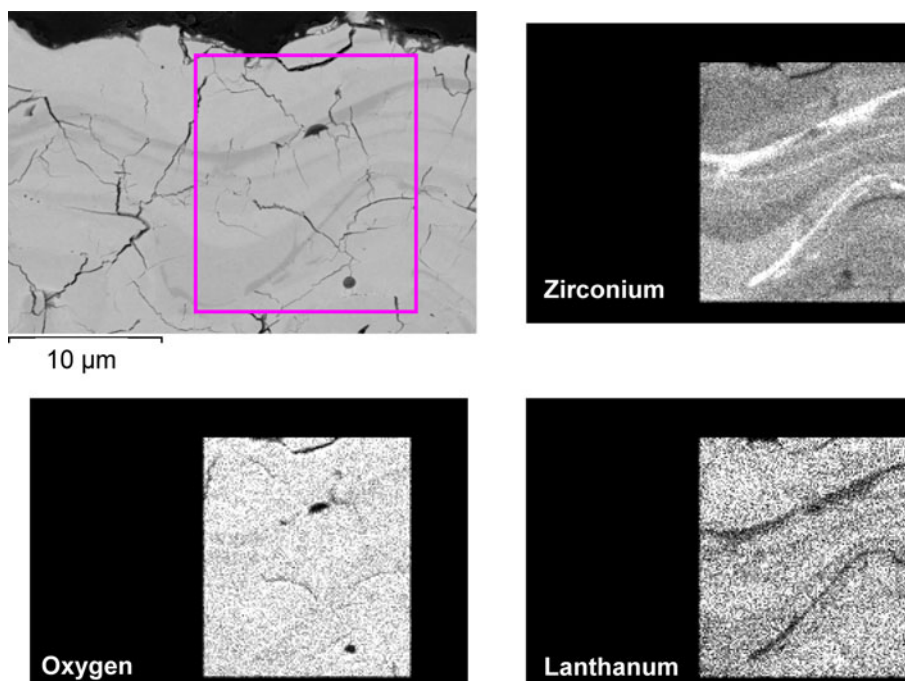
Fig. 7 SEM image (backscattered electrons) and EDS elemental mapping of oxygen, zirconium and lanthanum in the as-sprayed LZ coating at highest applied torch input power of 51 kW
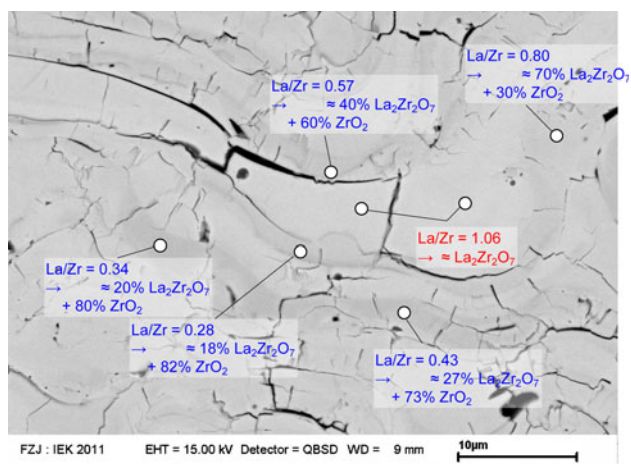

Fig. 8 SEM image (backscattered electrons) and quantitative EDS elemental point analyses of the as-sprayed LZ coating at highest torch input power of 51 kW. The indicated La/Zr ratios are atomic ratios, the percentages are mol%

lower torch input power do not show such pronounced lanthanum-depleted zones. Typically, under such conditions the porosity is larger and some small areas of partially unmelted particles are visible.

Quantitative EDS point analyses of the coatings sprayed at the highest torch power prove that the darker zones represent areas with considerable lanthanum depletion resulting in large amounts of zirconia along with the lanthanum zirconate (Fig. 8). Very low La/Zr atomic ratios down to 0.28 were found corresponding to zirconia contents of up to 82 mol% with only 18 mol% lanthanum

zirconate. The zones with intense lanthanum depletion are found at the splat peripheries. This is a clear indication that lanthania is lost by evaporation during flight since its vapor pressure is considerably higher than that of zirconia. Consequently, significant amounts of metastable cubic zirconia can develop. This is confirmed by x-ray diffractograms of annealed coatings sprayed at low and high torch power (Fig. 9). During annealing for 4 h at 1400 °C, the fluorite transforms to pyrochlore phase and, in particular, the sample sprayed at high torch power develops monoclinic and metastable zirconia phases which will transform and then undergo specific volume changes during thermal cycling. Consequently, the coating will fail very early. One example of a thermally cycled sample is shown in Fig. 10. The surface temperature was 1400 °C, the bondcoat temperature 1040 °C, and the lifetime was only 14 cycles.

3.4 Monitoring Melting, Evaporation and Solidification During Spray Process

Most of the particle temperature distributions measured in flight for the lower range of torch input power between 15.0 and 21.9 kW, as well as for higher torch input powers between 24.5 and 35.6 kW, show multimodal shapes, Fig. 11 and 12, respectively. Hence, the distributions are fitted with Gaussian functions to identify different particle fractions. At low power, two peaks can be identified for LZ; one at constant temperature (2570 °C at 15.0 and 17.3 kW) and another one at slightly increasing temperature (2624 °C at 15.0 kW, 2649 °C at 17.3 kW, 2650 °C at 19.6 kW, and 2656 °C at 21.9 kW). These peaks disappear at higher torch input power. For GZ, only one

such peak at almost constant temperature (2556-2584 °C) is observed between 19.6 and 25.4 kW.

Two further peaks appear at variable temperatures for both LZ and GZ. Regarding LZ, one of these peaks oc-
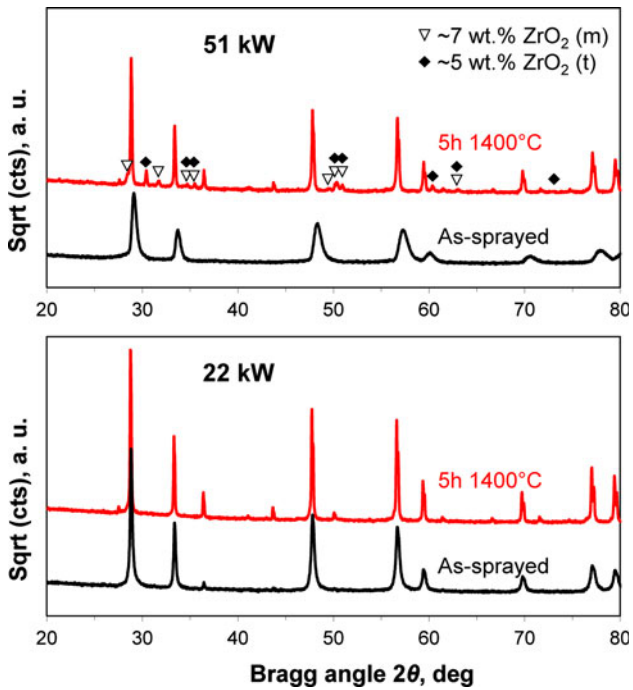

Fig. 9 X-ray diffractograms of annealed coatings sprayed at low and high torch power
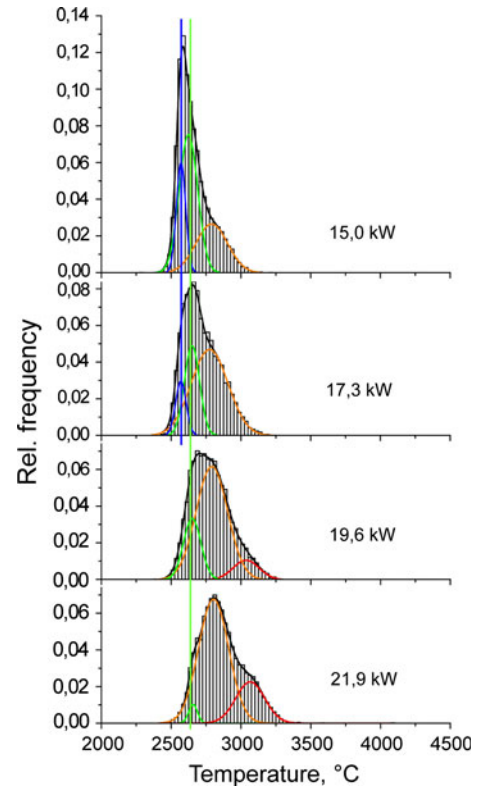

Fig. 11 LZ particle temperature distributions as estimated using two-color pyrometry for the lower range of torch input power between 15.0 and 21.9 kW
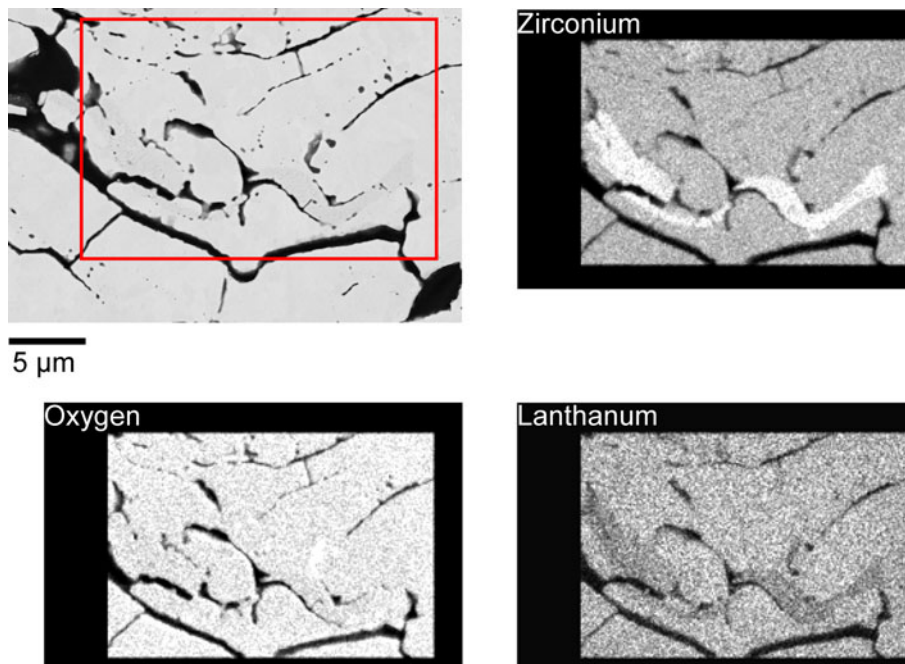

Fig. 10 EDS elemental mapping of thermally cycled coating sprayed at 52 kW
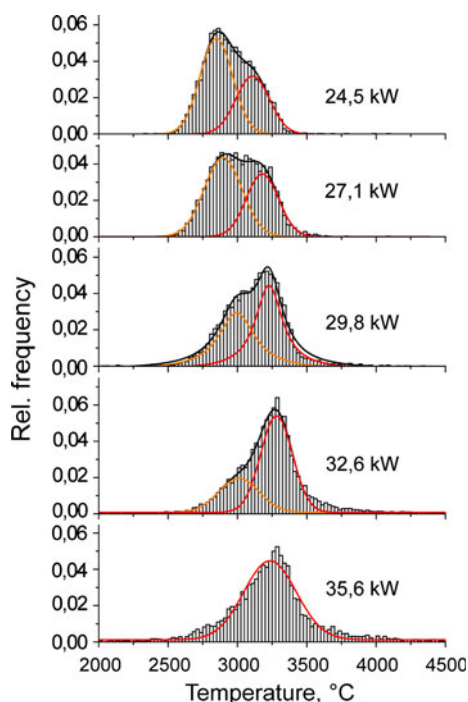
Fig. 12 LZ particle temperature distributions as estimated using two-color pyrometry for higher torch input powers between 24.5 and 36.5 kW

curs from the beginning at 15.0 kW and vanishes above 32.6 kW, and the other one exists at 19.6 kW and above. Furthermore, above 32.6 kW the distributions are increasingly scattered. A similar development is observed using the spherical GZ powder (not shown in this paper), but at a higher power level and with less scattering.

In the lower range of torch input power, the first two LZ peaks at constant and almost constant temperature, respectively, are assumed to be associated with solidification and release of fusion enthalpy. The solidifying behavior of particles in flight is dependent on the lanthania evaporation (Fig. 13). If the lanthania loss is low, solidification occurs immediately above the eutectic line at 2220 °C. Considering the fact that the phase diagram is valid for the equilibrium case only, as well as the limited quantitative accuracy of the two-color pyrometry method applied, this temperature is in reasonable agreement with the measured peak temperature. In the case of more intense lanthania evaporation, the solidification temperature is raised as is reflected by the second peak moving to higher temperatures.

In contrast, the slope of the GZ liquidus line in the phase diagram is small. Thus, the solidification temperature is hardly dependent on the gadolinia content so that only one peak at almost constant temperature is observed in the particle temperature distributions. The mean temperatures of this peak are in good agreement with the theoretical GZ melting temperature of approximately 2600 °C.
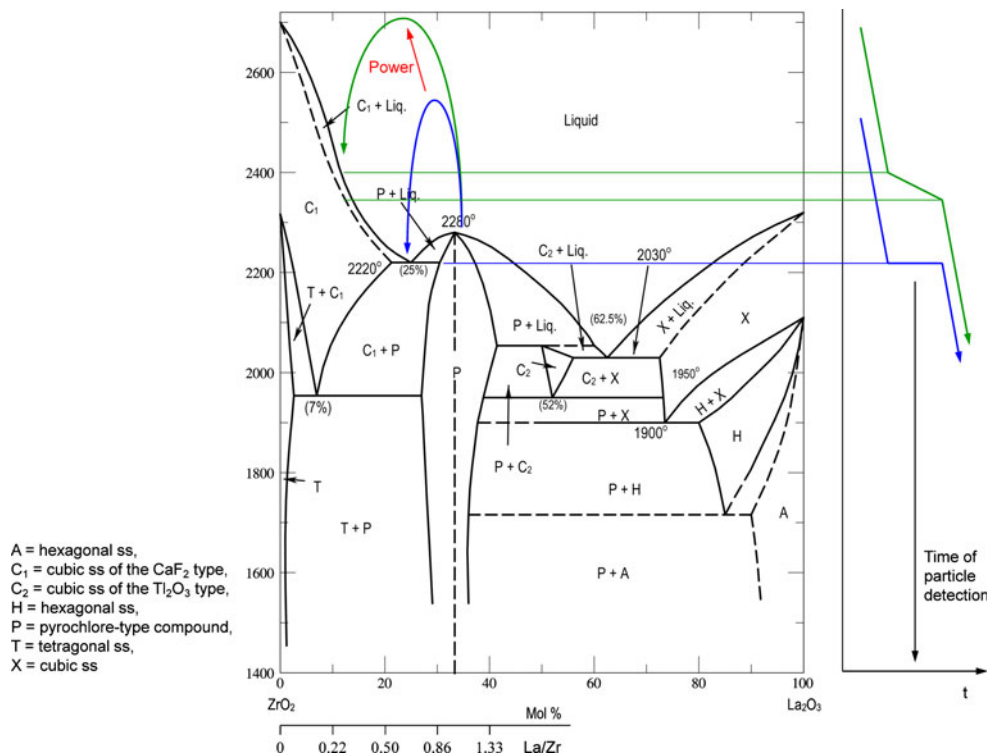

Fig. 13 Solidifying behavior of LZ particles in flight as a function of the lanthania content, phase diagram redrawn after (Ref 17)
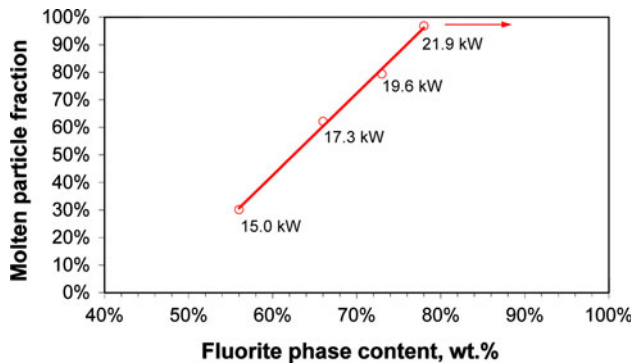
Fig. 14 Correlation of the fluorite contents derived from XRD with the molten LZ particle fractions determined by particle in-flight diagnostics

The two other distributions at variable temperatures in both the LZ and GZ cases are associated with molten particles. The reason for the appearance of two distributions is assumed to be the change of the composition at the radiating particle periphery due to the rare earth oxide evaporation. The remaining zirconia is assumed to have different emissivities compared to the zirconates. Thus, the results of two-color pyrometry are affected. Furthermore, if evaporation is intense, the particle radiation is scattered by vapor clouds so that the particle distributions are spread and scattered. This is evident in particular for LZ at 35.6 kW and above.

For LZ, the measured in-flight particle temperature distributions were also evaluated quantitatively. For the four lowest power levels applied (15.0-21.9 kW, this corresponds to the power range for which the particles were observed to be partly solidifying in flight), the different particle fractions were determined by calculating the areas under the Gaussian distributions. The amounts of material still molten show a strong linear correlation with the fluorite phase contents revealed by XRD (Fig. 14). Thus, the assumption is confirmed that such LZ material which is still molten upon impingement on the substrate is deposited as fluorite phase while the balance which has already solidified during flight may form pyrochlore.

4. Conclusion

Lanthanum zirconate tends to experience the evaporation of lanthania during plasma spraying. Above a specific power level, more lanthania is evaporated at the particle surfaces during flight so that lanthanum-depleted zones occur in the deposited coatings at the splat peripheries. As a consequence, unstabilized zirconia is formed and these non-stoichiometries are expected to be detrimental for applications in thermal barrier coatings. Thus, lanthania evaporation during spraying must be prevented as much as possible.

Based on these results, plasma spray parameters can be identified for the manufacture of stoichiometric lanthanum zirconate thermal barrier coatings so that the advantages of this material may be exploited. Particle

diagnostics were found to be an effective tool to detect and monitor lanthania evaporation during the spray process. The composition of the deposited coatings can be analyzed on the basis of lattice parameters obtained by XRD and Rietveld refinement.

References

1. A. Feuerstein, J. Knapp, T. Taylor, A. Ashary, A. Bolcavage, and N. Hitchman, Technical and Economical Aspects of Current Thermal Barrier Coating Systems for Gas Turbine Engines by Thermal Spray and EBPVD: A Review, *J. Therm. Spray Tech.*, 2008, **17**(2), p 199-213
2. R. Vaßen, H. Kaßner, A. Stuke, F. Hauler, D. Hathiramani, and D. Stöver, Advanced Thermal Spray Technologies for Applications in Energy Systems, *Surf. Coat. Technol.*, 2008, **202**, p 4432-4437
3. S. Stecura, *Effects of Compositional Changes on the Performance of a Thermal Barrier Coating System*, NASA TM-78976, National Aeronautics and Space Administration, 1978
4. R.A. Miller, J.L. Smialek, and R.G. Garlick, Phase Stability in Plasma-Sprayed, Partially Stabilized Zirconia-Yttria, *Advances in Ceramics*, Vol 3, *Science and Technology of Zirconia*, A.H. Heuer and L.W. Hobbs, Ed., The American Ceramic Society, Columbus, OH, 1981, p 241-253
5. D. Zhu and R.A. Miller, Thermal Conductivity and Elastic Modulus Evolution of Thermal Barrier Coatings Under High Heat Flux Conditions, *J. Therm. Spray Tech.*, 2000, **9**, p 175-180
6. R. Vaßen, A. Stuke, and D. Stöver, Recent Developments in the Field of Thermal Barrier Coatings, *J. Therm. Spray Tech.*, 2009, **18**(2), p 181-186
7. R. Vaßen, X.Q. Cao, F. Tietz, D. Basu, and D. Stöver, Zirconates as New Materials for Thermal Barrier Coatings, *J. Am. Ceram. Soc.*, 2000, **83**(8), p 2023-2028
8. D.R. Clarke and S.R. Phillpot, Thermal Barrier Coating Materials, *Mater. Today*, 2005, **8**(6), p 22-29
9. R. Vaßen, M.O. Jarligo, T. Steinke, D.E. Mack, and D. Stöver, Overview on Advanced Thermal Barrier Coatings, *Surf. Coat. Technol.*, 2010, **205**, p 938-942
10. X.Q. Cao, R. Vaßen, and D. Stöver, Ceramic Materials for Thermal Barrier Coatings, *J. Eur. Ceram. Soc.*, 2004, **24**, p 1-10
11. H. Lehmann, D. Pitzer, G. Pracht, R. Vaßen, and D. Stöver, Thermal Conductivity and Thermal Expansion Coefficients of the Lanthanum Rare-Earth-Element Zirconate System, *J. Am. Ceram. Soc.*, 2003, **86**(8), p 1338-1344
12. M.M. Gentleman and D.R. Clarke, Luminescence Sensing of Temperature in Pyrochlore Zirconate Materials for Thermal Barrier Coatings, *Surf. Coat. Technol.*, 2005, **200**, p 1264-1269
13. R. Vaßen, F. Traeger, and D. Stöver, New Thermal Barrier Coatings Based on Pyrochlore/YSZ Double-Layer Systems, *Int. J. Appl. Ceram. Technol.*, 2004, **1**(4), p 351-361
14. X.Q. Cao, R. Vaßen, F. Tietz, and D. Stöver, New Double-Ceramic-Layer Thermal Barrier Coatings Based on Zirconia-Rare Earth Composite Oxides, *J. Eur. Ceram. Soc.*, 2006, **26**, p 247-251
15. H. Chen, Y. Liu, Y. Gao, S. Tao, and H. Luo, Design, Preparation, and Characterization of Graded YSZ/La₂Zr₂O₇ Thermal Barrier Coatings, *J. Am. Ceram. Soc.*, 2010, **93**(6), p 1732-1740
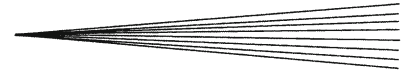
16. X.Q. Cao, R. Vaßen, W. Jungen, S. Schwartz, F. Tietz, and D. Stöver, Thermal Stability of Lanthanum Zirconate Plasma-Sprayed Coating, *J. Am. Ceram. Soc.*, 2001, **84**(9), p 2086-2090

17. A. Rouanet, Contribution a l'étude des systèmes zircone-oxydes des lanthanides au voisinage de la fusion, *Revue Internationale des Hautes Températures et des Réfractaires*, 1971, **9**(2), p 161/80. In: ACerS-NIST Phase Equilibria Diagrams, CD-ROM Database V. 3.1.0, American Ceramic Society, Westerville, OH, USA, 2005

18. A.V. Radha, S.V. Ushakov, and A. Navrotsky, Thermochemistry of Lanthanum Zirconate Pyrochlore, *J. Mater. Res.*, 2009, **24**(11), p 3350-3357

19. R. Vaßen, Entwicklung neuer oxidischer Wärmedämmschichten für Anwendungen in stationären und Flug-Gasturbinen, *Schriften des Forschungszentrums Jülich, Energy Technology*, Vol 33, Forschungszentrum Jülich, 2004 (in German)

20. H. Chen, Y. Gaoa, Y. Liua, and H. Luo, Coprecipitation Synthesis and Thermal Conductivity of $La_2Zr_2O_7$, *J. Alloys Compd.*, 2009, **480**, p 843-848

21. H. Chen, Y. Gao, S. Tao, Y. Liu, and H. Luo, Thermophysical Properties of Lanthanum Zirconate Coating Prepared by Plasma Spraying and the Influence of Post Annealing, *J. Alloys Compd.*, 2009, **486**, p 391-399

22. Z. Xu, L. He, R. Mu, S. He, and X. Cao, Preparation and Characterization of $La_2Zr_2O_7$ Coating with the Addition of Y_2O_3 by EB-PVD, *J. Alloys Compd.*, 2010, **492**, p 701-705

23. J.L. Margrave, Ed., *The Characterization of High Temperature Vapors*, Wiley, New York, NY, 1967

24. R.J. Meyer, E.H.E. Pietsch, A. Kotowski, M. Becke-Goehring, and K.-C. Buschbeck, *Gmelin Handbuch der Anorganischen Chemie*, 8th ed., Springer-Verlag, Berlin, 1974 (in German)

25. W. Goldstein, P.N. Walsh, and D. White, Rare Earths. I. Vaporization of La_2O_3 and Nd_2O_3: Dissociation Energies of Gaseous LaO and NdO, *J. Phys. Chem.*, 1960, **65**, p 1400-1404

26. G. Mauer, R. Vaßen, and D. Stöver, Comparison and Applications of DPV-2000 and Accuraspray-g3 Diagnostic Systems, *J. Therm. Spray Tech.*, 2007, **16**, p 414-424

27. H.M. Rietveld, A Profile Refinement Method for Nuclear and Magnetic Structures, *J. Appl. Crystallogr.*, 1969, **2**, p 65-71

28. L. Vegard, Die Konstitution der Mischkristalle und die Raumfüllung der Atome, *Z. Phys.*, 1921, **5**(1), p 17-26 (in German)